Received: 5 May 2022 | Revised: 13 February 2023 | Accepted: 21 March 2023

DOI: 10.1002/nbm.4947

RESEARCH ARTICLE

NMR IN BIOMEDICINE WILEY

Estimation of subvoxel fat infiltration in neurodegenerative muscle disorders using quantitative multi-T_2 analysis

Jannette Nassar[1] | Amira Trabelsi[2] | Rula Amer[1] | Yann Le Fur[2] | Shahram Attarian[3,4] | Dvir Radunsky[1] | Tamar Blumenfeld-Katzir[1] | Hayit Greenspan[1] | David Bendahan[2] | Noam Ben-Eliezer[1,5,6]

[1]Department of Biomedical Engineering, Tel Aviv University, Tel Aviv, Israel

[2]Aix Marseille University, Marseille, France

[3]Reference Center for Neuromuscular Diseases and ALS, La Timone University Hospital, Aix-Marseille University, Marseille, France

[4]Inserm, GMGF, Aix Marseille University, Marseille, France

[5]Sagol School of Neuroscience, Tel Aviv University, Tel Aviv, Israel

[6]Center for Advanced Imaging Innovation and Research, New York University Langone Medical Center, New York, New York, USA

Correspondence
Noam Ben-Eliezer, Department of Biomedical Engineering, Tel Aviv University, Tel Aviv 6997801, Israel.
Email: noambe@tauex.tau.ac.il

Funding information
This research was funded by the ISF Grant 2009/17, and the CNRS and APHM.

Abstract

MRI's T_2 relaxation time is a valuable biomarker for neuromuscular disorders and muscle dystrophies. One of the hallmarks of these pathologies is the infiltration of adipose tissue and a loss of muscle volume. This leads to a mixture of two signal components, from fat and from water, to appear in each imaged voxel, each having a specific T_2 relaxation time. In this proof-of-concept work, we present a technique that can separate the signals from water and from fat within each voxel, measure their separate T_2 values, and calculate their relative fractions. The echo modulation curve (EMC) algorithm is a dictionary-based technique that offers accurate and reproducible mapping of T_2 relaxation times. We present an extension of the EMC algorithm for estimating subvoxel fat and water fractions, alongside the T_2 and proton-density values of each component. To facilitate data processing, calf and thigh anatomy were automatically segmented using a fully convolutional neural network and FSLeyes software. The preprocessing included creating two signal dictionaries, for water and for fat, using Bloch simulations of the prospective protocol. Postprocessing included voxelwise fitting for two components, by matching the experimental decay curve to a linear combination of the two simulated dictionaries. Subvoxel fat and water fractions and relaxation times were generated and used to calculate a new quantitative biomarker, termed viable muscle index, and reflecting disease severity. This biomarker indicates the fraction of remaining muscle out of the entire muscle region. The results were compared with those using the conventional Dixon technique, showing high agreement ($R = 0.98$, $p < 0.001$). It was concluded that the new extension of the EMC algorithm can be used to quantify abnormal fat infiltration as well as identify early inflammatory processes corresponding to elevation in the T_2 value of the water (muscle) component. This new ability may improve the diagnostic accuracy of neuromuscular diseases, help stratification of patients according to disease severity, and offer an efficient tool for tracking disease progression.

Abbreviations: EMC, echo modulation curve; EPG, extended phase graph; ETL, echo train length; FCNN, fully convolutional neural network; MESE, multi-echo spin-echo; qT_2, quantitative T_2; ROI, region of interest; SC, subcutaneous; SE, spin-echo; VMI, viable muscle index.

KEYWORDS
fat fraction, fat infiltration, muscle dystrophy, quantitative magnetic resonance imaging, transverse relaxation time T_2

1 | INTRODUCTION

MRI's transverse relaxation time (T_2) has been proposed as a biomarker of neuromuscular disorders, and as an indicator of treatment response.[1,2] This relaxation time manifests both macrostructural (voxel level) and microstructural (subvoxel) tissue changes, making it a proxy for peripheral muscle dystrophies, inflammatory processes, or neuromuscular disorders. One of the hallmarks of these disorders is the substitution of muscular tissue by fat and connective tissue, and a subsequent loss of muscle volume. The MRI signal from such a mixture of muscle and fat will therefore reflect a superposition of two components within each imaged voxel: the first originating from intrafilamentary water molecules in muscle, and the second associated with protons in the methylene group in fat molecules.[3] Quantification of these fat and muscle components thus holds great diagnostic and prognostic value by enabling accurate assessment of muscle state and staging of disease progression.[4,5]

One of the early techniques for estimating fat and muscle-water fractions (f_{fat} and f_{water}) was developed by Dixon et al.[6,7] This approach relies on collecting two separate spin-echo (SE) images, one where the signals from water and from fat protons are in phase, and a second image with them 180° out-of-phase (termed the two-point Dixon technique). The relative fractions of water and fat can then be determined by adding and subtracting the two images, yielding water and fat fraction (FF) maps. An extension of this technique to accommodate three echo times is also available (i.e., the three-point Dixon technique), allowing to overcome potential fat/water swap errors in voxels with a high fat infiltration level, and in order to correct for phase errors caused by inhomogeneities of the main magnetic field B_0.[8]

Another approach for estimating fat and water fractions employs multiecho spin-echo (MESE) protocols, which allows to separate the fat and muscle-water components based on differences in their T_2 relaxation times.[9–12] A natural and important prerequisite of probing two T_2 components is to be able to achieve reliable quantification of single T_2 values. This task, however, is by itself challenging in clinical settings because of the bias of MESE protocols by stimulated and indirect echoes.[13] These cause MESE signals to deviate from the theoretical exponential T_2 decay pattern, and instead follow a more generalized echo modulation curve (EMC).[14,15] This deviation is moreover not constant across different T_2 values, protocol implementations, and scan parameters, causing T_2 values for a given subject to vary between scanners and scan settings.[16] Single- or multi-exponential fitting models of MESE data may thus produce unreliable values as they do not account for stimulated echoes.[12]

Two simple approaches to alleviate some of the signal bias caused by stimulated and indirect echoes are to remove the first echo or to use only the even numbered echoes. Apart from omitting high signal-to-noise ratio (SNR) datapoints, both of these solutions still do not provide an accurate measure of T_2 for two reasons: (1) the indirect echoes affect the entire T_2 decay curve, and (2) the T_2 decay curve still depends on the scan parameters and will change, for example, when changing the slice thickness, acquisition bandwidth, excitation/refocusing RF pulse shapes, and flip angles, etc.

Another possible approach for overcoming this bias is provided by the extended phase graph (EPG) formalism,[17] which tracks all the coherence pathways in the MESE echo train to calculate a more realistic experimental decay curve. An extension of the EPG method for a two-component signal model has been reported recently to estimate the muscle transverse relaxation time and FF in thigh muscle of patients with various neuromuscular diseases.[18,19] Another recent approach is magnetic resonance fingerprinting (MRF). This multiparametric mapping technique uses a pseudo-randomized acquisition scheme to generate a signal fingerprint, which is then fitted to a precalculated dictionary of simulated signal curves in order to extract the parameters encoded during the experiment.[20,21] An extension of the MRF framework for two components has been developed recently,[22] demonstrating its ability to generate FF maps alongside other tissue properties such as T_1 and T_2 relaxation times.[22] The main limitation of MRF-based separation of fat and water is the error in FF in the presence of main field (B_0) inhomogeneities.

The EMC algorithm has been proposed for accurate and stable mapping of T_2 relaxation times.[15,16] This algorithm uses Bloch simulations to model the magnetization evolution during multiecho acquisitions, followed by a dictionary-matching fitting process. The EMC technique has been shown to correctly model MESE signals and deliver accurate and reliable maps of the tissues' T_2 values. Notably, the fitted values are reproducible and, most importantly, independent of the sca'ner, scan settings, and protocol implementation.[23]

The EPG'and EMC algorithms are based on SE protocols and are thus immune to B_0 inhomogeneities. MRF on the other hand is based on fast gradient-echo acquisitions so as to accelerate data acquisition, yet at a cost of lower T_2 encoding quality and sensitivity to B_0 inhomogeneities vis-à-vis SE-based acquisitions.

In this current proof-of-concept study, we report an extension of the EMC algorithm for two-component fitting focusing on subvoxel estimation of fat and water fractions, alongside their T_2 relaxation times. The advantage of using the extended EMC framework is its ability to quantify the amount of infiltrated fat in a muscle tissue, while at the same time probing changes in muscle T_2 values that are indicative of underlying inflammatory or fibrotic processes.[1,2] Examples of the extended EMC algorithm are shown for healthy subjects, patients suffering from muscular

dysferlinopathy, and patients with Charcot–Marie-Tooth (CMT) disease. The results are validated against Dixon-based estimations of water and fat fractions.

2 | METHODS

2.1 | Study population

Five healthy volunteers (age 35 ± 8 years) were scanned at the MRI facility at Tel Aviv University. An informed consent form was signed by all volunteers and the study was approved by the local ethics committee. Two patients (age 38.5 ± 0.5 years) with a genetically confirmed dysferlinopathy, and 11 patients (age 57 ± 15 years) with genetically confirmed CMT disease, were recruited and scanned at the Centre de Résonance Magnétique Biologique et Médicale in Marseille, France. All patients' scans were approved by the local ethics committee (Comité de Protection des Personnes Sud Méditerranée I).

2.2 | MRI scans

Volunteer scans of the calf muscle were carried out on a whole-body 3-T scanner (Prisma, Siemens Healthineers). Dysferlinopathy and CMT patients were scanned on a whole-body 1.5-T scanner (Avanto, Siemens Healthineers). All subjects were scanned in supine position (feet first) using an eight-channel flexible matrix coil. Scans included a single-voxel spectroscopy (SVS), a two- and three-point Dixon, and a MESE protocol. SVS scans used the STRESS protocol[24] (see the supporting information, Section S5). The STRESS scan parameters were T_{acq} = 1 h 3 min; voxel size = 20 x 20 x 15 mm^3; TR = 1500 ms; TE = 15 ms; and $N_{Averages}$ = 32. The three-dimensional two-point Dixon scan parameters were TR = 30 ms; TE1/TE2 = 2.46/3.69 ms; flip angle = 15°; N_{slabs} = 1 covering the central part of the calf anatomy (one readout dimension and two phase-encoded dimensions); slices per slab = 16; voxel size = 1.1 x 1.1 x 4.0 mm^3 (slice thickness = 4 mm); coverage = 64 mm; $N_{Averages}$ = 3; T_{acq} = 1 h 10 min; and acceleration = 2 x CAIPIRINHA. The three-dimensional three-point Dixon scan parameters were TR = 22 ms; TE1/TE2/TE3 = 2.38/4.76/7.16 ms; flip angle = 5°; N_{Slabs} = 1 covering the central part of the calf/thigh anatomies; slices per slab = 36; voxel size = 1.72 x 1.72 x 5.0 mm^3 (slice thickness = 5 mm); coverage = 180 mm; $N_{Averages}$ = 2; T_{acq} = 3 h 23 min; and acceleration = 2 x CAIPIRINHA. The MESE scan used a 2D multislice acquisition while the FOVs were positioned so as to cover the entire calf/thigh muscle regions. The MESE protocol parameters for volunteers, dysferlinopathy, and CMT patients, respectively, were TR/TE = 3000/10, 2500/8.7, and 2500/8.7 ms; N_{Echoes} = 25, 17, and 16; voxel size = 1.1 x 1.1, 1.5 x 1.5, and 1.7 x 1.7 mm^2; slice thickness = 4, 10, and 10 mm; N_{slices} = 5, 5, and 10; slice gap = 6, 30, and 20 mm; coverage = 28, 130, and 190 mm; T_{acq} = 3 h 18 min, 2 h 28 min, and 3 h 8 min; and acceleration = x2 GRAPPA. Fully convolutional neural network (FCNN) training used MESE data from the thighs and calves of 14 dysferlinopathy patients (age 36 ± 4 years). The scan parameters were TR/TE = 1479/8.7 ms; N_{Echoes} = 17; in-plane resolution = 1.5 × 1.5 mm^2; matrix size of 128 × 128; N_{slices} = 5; slice thickness = 10 mm; and T_{acq} = 5 h 7 min.

2.3 | Data postprocessing

Spectroscopic quantification of water and fat content was carried out by calculating the area under each peak in the SVS spectra as a percentage of the total area under all peaks. Peaks were identified with a constraint of a 0.2 ppm minimal distance between the water and fat peak in the spectrum (as the water found at 4.7 ppm is at least 3.5 ppm apart from the methylene fat peak found at ∼1.2 ppm). A threshold was applied to exclude peaks that were less than 6% from the spectra's maximum value. The ground truth reference T_2 values were calculated from the series of SVS scans performed at increasing TEs. The water fraction was quantified from the SVS spectrum by taking the integral under the water peak at 4.7 ppm. Peak areas were then plotted against their corresponding TEs, producing an exponential decay curve, and the ground truth muscle/water T_2 value was calculated from that exponential curve. Dixon water and fat fractions were determined using the two-point Dixon technique for volunteers[7] and using the three-point Dixon technique for patients.[8]

2.4 | Segmentation of images using a FCNN

Prior to applying the extended EMC algorithm, the anatomical MR images of the calf were segmented to identify the clinically relevant region of interest (ROI) for muscle dystrophies. This covered the healthy and diseased muscle regions, and excluded the subcutaneous (SC) fat, the intermuscular fascia, and the bones. The first stage of segmentation consisted of delineating the muscle's outer boundary on the raw (T_2-weighted)

MESE images using a Canny edge detector. The images were then normalized to zero mean and unit variance. The resulting mask was then used as an input to a fully convoluted deep learning neural network. Network training data consisted of calf and thigh muscle scans from 14 patients, manually segmented by an expert with more than 10 years of experience. These were concatenated and fed to the network's input via 17 channels corresponding to the number of timepoints in the MESE protocol echo train. The model was trained using the Adam optimizer, with the default settings for the tested machine learning problem as follows: $\alpha = 0.001$, $\beta 1 = 0.9$, $\beta 2 = 0.999$, and $\epsilon = 10^{-8}$.[25] The optimized loss function was the Dice coefficient loss. The batch size was set to 8 and the model was trained for 100 epochs. To improve the model's robustness in the presence of data variance, augmentation was performed on the original training images, increasing their number by a factor of 10. This summed up to a total of 14 (patients) x 5 (slices per patient) x 17 (echoes) x 10 (augmentations) = 11,900 slices used for the training process. The augmentation included shifting the training images (0.2 of image height and width), zooming (from 0.9 to 1.3 of image size), rotating (0°−30°), and flipping (vertical\horizontal). The network implementation was written in Python and used the Keras libraries. The training process of the neural network was performed on a standard PC with an NVIDIA GeForce GTX 1080 Ti GPU.[26]

The network used is a convolutional network for medical image segmentation, otherwise known as a U-Net. The network output consisted of a muscle mask (including any infiltrated fat) and a second mask containing the SC fat and the bones. Testing of the FCNN was performed on a dataset consisting of three patients with different disease severities. The evaluation metrics used to assess the performance of the network were the Dice similarity coefficient (DSC) = (2 x TP)/(2 x TP + FP + FN), positive predictive value (PPV) = TP/(TP + FP), specificity = TN/(TN + FP), and sensitivity = TP/(TP + FN), where TP = true positive, TN = true negative, FP = false positive, and FN = false negative. A summary of the network architecture and performance is given in supporting information Sections S1 and S2.

The thigh muscles of the 11 CMT patients were segmented by our FCNN (to separate it from the SC fat) and was then delineated into 10 different muscle regions: vastus intermedius, vastus lateralis, vastus medialis, rectus femoris, adductor, semimembranous, semitendinous, biceps femoris, sartorius, and gracilis muscles. This was done automatically using FSLeyes imaging software developed by the FMRIB Centre at the University of Oxford.[27]

2.5 | The extended EMC algorithm – generation of fat/water fraction maps

Programming of the extended EMC algorithm was done in-house using MATLAB (MathWorks Inc., Natick, MA, USA) and C++. Preprocessing involved creating a dictionary of signal decay curves by repeating Bloch simulations of the prospective MESE protocol for T_2 relaxation values in the range 5–1000 ms (generic dictionary used for all organs), and transmit-field (B_1^+) inhomogeneity levels of 70%–130% of nominal value. This produced a dictionary ($\mathbb{D}_{\text{Water}}$) of simulated EMCs, labeled EMC_{Water}, each associated with a unique pair of $[B_1^+, T_2^W]$ values, where $T_2^W = T_2$ of water component. A second dictionary was created for the fat component, that is, for the signal originating from protons in the CH_2 (methylene) groups, having the highest natural abundance in a fat molecule. This dictionary ($\mathbb{D}_{\text{Fat}}$) was generated by repeating the above simulations, but at 3.5 ppm (447 Hz) off-resonance. Each EMC in the $\mathbb{D}_{\text{Fat}}$, labeled EMC_{Fat}, was similarly associated with a unique pair of $[B_1^+, T_2^F]$, where $T_2^F = T_2$ of fat component (Figure S3).

Postprocessing was done on a voxel-by-voxel basis by matching the experimental EMC to a linear combination of the two simulated dictionaries. This was calculated as the weighted sum of two decay curves

$$EMC_{experimental} = f_W \times EMC_{Water} + (1 - f_W) \times EMC_{Fat}, \quad (1)$$

where f_W is the water fraction in the range 0%–100% with increments of 2%, resulting in three parametric maps, T_2^W, T_2^F, and f_W. Fitting of the signal in each voxel was done via L2-norm minimization of the difference between the experimental and the simulated EMCs, over the range of simulated $[B_1^+, T_2^W, T_2^F, f_W]$ values, and choosing the dictionary entry that yields the minimum norm. Experimental signal timepoints with an intensity below a 10% threshold were truncated to avoid bias due to Rician noise at the signal tail.[28] The large difference between the short water T_2 and long fat T_2 values caused the water component's signal to decay much more rapidly than the fat signal. As a result, the number of timepoints in the L2-norm calculation needed to be adjusted to take only the number of meaningful points of each component and exclude noisy datapoints. To that end, the experimental EMC was separated into two components by subtracting the simulated water signal from the experimental curve to produce fat-only signal and subtracting the simulated fat signal to produce water-only signal. Two L2 norms were then calculated separately for water and for fat signals and then summed according to each component's relative fraction to produce a final L2 norm value. A flowchart of the extended EMC algorithm is illustrated in Figure 1. The ambiguity of this three-parameter fitting method was overcome in step (c) by fixating the fat T_2 value (allowing it a smaller range), which greatly improved the convergence of the fitting process.

The algorithm included four main steps. Step (a): automatic segmentation using an FCNN,[29] producing a mask of the muscle region, including any infiltrated fat (excluding the bones), and a second mask of the SC fat region. Step (b): a standard, single-T_2 component EMC fitting of the muscle region outputted from step (a). The resulting B_1^+ map was then spatially extrapolated to yield a B_1^+ map of the entire anatomy (i.e., all muscles and SC fat). Step (c): a two-component fit was performed on the SC fat region only outputted from step (a). Fat fraction in this region was set to

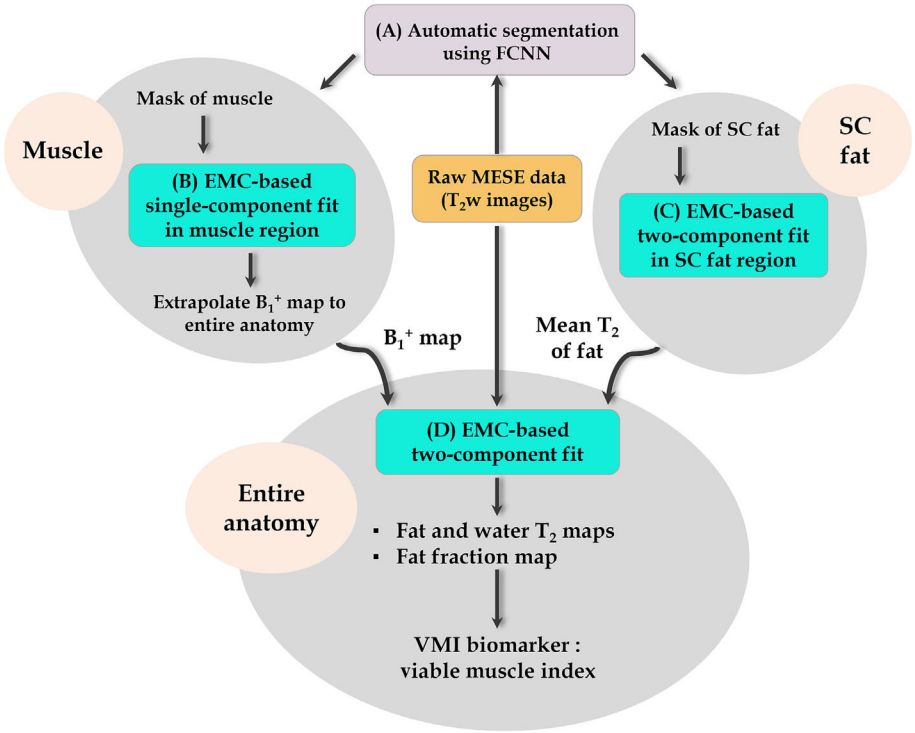

FIGURE 1 Flowchart of the extended EMC algorithm used for fat/water estimation. (A) The raw MESE data are initially inputted into a fully convolutional neural network (FCNN) that segments the anatomy to muscle regions and subcutaneous (SC) fat, while excluding the bones and bone marrow. (B) A simple single-T_2 component fit is performed in the muscle region, producing a B_1^+ map which is then extrapolated to cover the entire anatomy. (C) A two-component fit is then performed within the subcutaneous fat region to calculate the T_2 value of fat in the examined anatomy. (d) T_2^W, T_2^F, and f_W maps are calculated by performing a two-component fit of the segmented anatomy (muscle and infiltrated fat region), yielding the clinical VMI biomarker. EMC, echo modulation curve; MESE, multiecho spin-echo; T_2w, T_2-weighted.

90% ($f_W = 10\%$), based on a previous report by.[12] The mean $\overline{T_2^F}$ of fat computed in this step was assumed to represent the baseline T_2^F in the entire anatomy and was used as input to the next step. Step (d): a two-component fit was performed for the segmented muscle anatomy (muscle + infiltrated fat). The allowed range of fat T_2 values was set to $\overline{T_2^F}$ of fat from step (c), ± 0.3 x standard deviation (SD) as a prior to the fitting process. This 30% margin was chosen to allow for natural deviations in the local T_2^F values. The fitting process consisted, in this case, of a three-parameter (T_2^F, T_2^W,f_W) fit of the experimental EMC to the combined fat-water dictionaries using an exhaustive search, that is, by sampling all possible combinations of T_2^F, T_2^W,and f_W. The closest simulated decay curve was then chosen according to two constraints. The first constraint was finding the minimum L2 norm difference between experimental and simulated EMCs. The second was a "single-T_2 validation constraint", demanding that the analytically constructed single-T_2 value computed by combining the T_2 values of the two components, as in Equation (2), falls within a 5% range of the empirical single-T_2 computed in step (a):

$$T_{2,analytical} = f_W \, x \, EMC_W \, x \, e^{\frac{-TE}{T_2^W}} + (1 - f_W) \, x \, EMC_F \, x \, e^{\frac{-TE}{T_2^F}}. \quad (2)$$

This procedure was performed for each voxel in the image, yielding T_2^W, T_2^F, and f_W maps (Section S4). A new quantitative biomarker for muscle health, termed the global viable muscle index (VMI), was then calculated to reflect a global measure of disease progression, by denoting the fraction of remaining muscle out of the entire muscle region. This marker might be useful as it provides a complementary measure of muscle volume.

3 | RESULTS

Application of the extended two-component EMC algorithm is illustrated in Figure 2, showing a water fraction map of a transverse slice of the calf muscle of a patient with dysferlinopathy. Good agreement is seen between the experimental and simulated decay curves (black asterisk and solid red line, respectively) for a representative voxel, marked with a red ROI. For reference, water-only and fat-only T_2 decay curves are shown in

dotted blue and dashed black lines, respectively. The water fraction in this diseased muscle voxel was found to be $f_{water} = 0.46$, with the rest of the voxel consisting of fat which replaced the muscle tissue.

Examples of the automatic segmentation stage are shown in supporting information, Section S2, Figure S2 for dysferlinopathy patients at three levels of disease severity. Section S1 and Table S1 summarize the network performance based on DSC, PPV, sensitivity, and specificity. All evaluation metrics produced highly positive values, reflecting the network's high performance. Results for mild, moderate, and severe disease levels were, respectively, DSC: 0.964, 0.973, and 0.963; PPV: 0.943, 0.994, and 0.950; sensitivity: 0.987, 0.952, and 0.975; and specificity: 0.990, 0.999, and 0.993.

Fat/water quantification in an axial slice of one of the healthy volunteers is shown in Figure 3 using the extended EMC algorithm (3b), Dixon (3c), and SVS (3d,e). An EMC-based water T_2 map is presented in Figure 3F. The water fraction in the muscle region (blue ROI in Figure 3A) was $f_{water} = 97.5\% \pm 1.1\%$, $97.7\% \pm 10.0\%$, and 96.8% for the three techniques, respectively. We consider these values to be in good agreement considering the natural interscan variations and the different encoding protocols of each technique.

Figure 4 demonstrates the application of the extended EMC algorithm on a patient with mild dysferlinopathy. Panel (a) shows an anatomical T_2-weighted image (TE = 17.4 ms), marked with a muscle region, which was automatically segmented by the deep learning U-Net (dashed line).

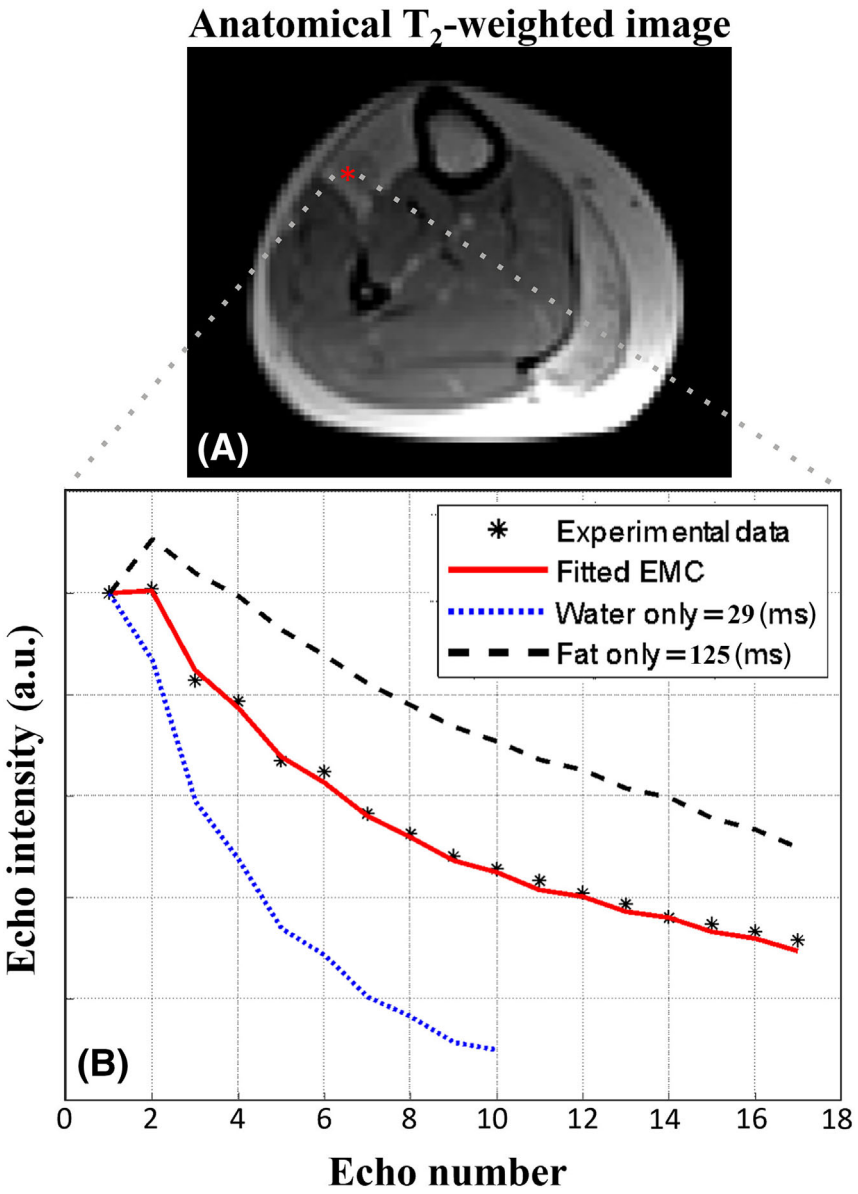

FIGURE 2 Two-T_2 component fit showing good agreement between experimental and simulated decay curves in a diseased muscle voxel (marked by the red asterisk in an anatomical T_2-weighted image in (A)) consisting of both water and fat molecules. (B) Water-only and fat-only T_2 decay curves are shown as dotted blue and dashed black lines, reflecting f_{water} of 0.46.

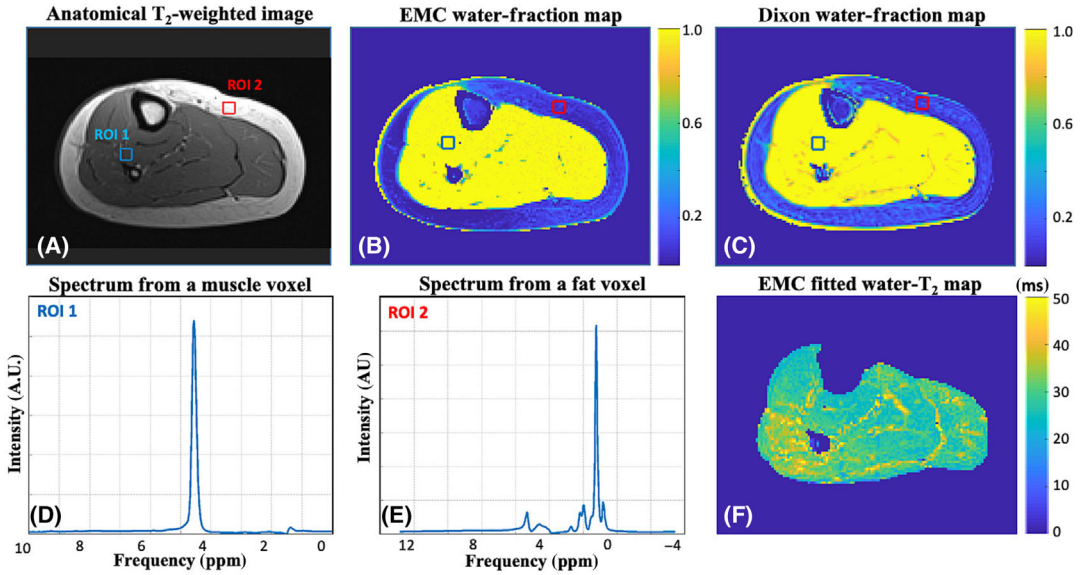

FIGURE 3 Two-T_2 component fit for an axial slice of a calf muscle from a healthy volunteer. FOVs for EMC and Dixon were positioned so as to overlap and cover the central parts of the calf muscles. (A) Anatomical T_2- weighted image. (B) f_W map produced by the EMC algorithm showing a mean value of $f_W = 97.5\% \pm 1.1\%$ in the muscle region (blue ROI) and a mean $f_W = 7.0\% \pm 3.0\%$ in the SC fat region (red ROI). (C) Dixon-based f_W map producing mean $f_W = 97.7\% \pm 10.0\%$ in the muscle region (blue ROI) and mean $f_W = 10.8\% \pm 6.2\%$ in the SC fat region (red ROI). (D) Single voxel spectroscopy (SVS) of a fat voxel producing 94.9% fat and 5.1% water. (E) SVS of a muscle voxel producing 96.8% water and 3.2% fat. (F) Quantitative map of the T_2 relaxation time for the water component only. EMC, echo modulation curve; FOV, field of view; ROI, region of interest; SC, subcutaneous.

Water fraction in a diseased muscle region (red square ROI) was f_{water} = 96.0% ± 8.1% and 94.0% ± 11.0%, calculated using the extended EMC algorithm (4b) and the Dixon technique (4c), respectively. The ground truth reference T_2 value was calculated from the SVS scans by fitting to an exponentially decaying model (see the Methods section), yielding a T_2 = 42.5 ms with R-square = 0.998 for the goodness of fit. An EMC-based water T_2 map is presented in Figure 4E, exhibiting a T_2 value of 38.1 ± 6.4 ms in this diseased muscle ROI, in agreement with the corresponding SVS value. The marked area reflects a typical dysferlinopathy pathology where fat has not yet replaced the muscle tissue, yet the T_2 of the diseased muscle was elevated based on the extended EMC algorithm.

Results for a patient with a moderate case of dysferlinopathy are shown in Figure 5. Water fraction maps calculated using the extended EMC algorithm (5b) and the Dixon technique (5c) demonstrate the infiltration of fat into the diseased muscle region. Panel (d) shows an EMC-based water T_2 map. The mean water fraction for an ROI located within the tibialis anterior muscle region (red ROI) was f_{water} = 22.6% ± 11.5% and 21.8% ± 8.3% using the EMC algorithm and the Dixon technique, respectively, both reflecting clear muscle degeneration. The corresponding FF maps are shown in Figure S6.

Mean FF for each muscle was calculated from the FF maps using both the extended EMC algorithm and the gold standard three-point Dixon technique. The correlation between the FF values calculated with both methods is shown in Figure 6A, producing $R^2 = 0.98$, indicating excellent correlation ($p < 0.001$), fitting the linear relation $y = -0.061 + 1.1x$. A Bland–Altman plot comparing the FFs derived from both methods is shown in Figure 6B. All values shown in Figures 6 and 7 are calculated from 2D data consisting of a series of transverse slices. The systemic mean bias was 0.043 (solid black line) in FF value between the two methods. The red dashed lines correspond to the 95% confidence intervals, and all the points fall within them, except for a few outliers.

The correlation between the muscle volume as calculated using both methods is shown in Figure 7A, producing a correlation of R2 = 0.98, indicating excellent agreement ($p < 0.001$), fitting the linear relation $y = -460 + 0.99x$. A Bland–Altman plot comparing the muscle volume derived from both methods is shown in Figure 7B. The mean bias in muscle volume measurement between the two assayed methods was 608 mm^3 (solid black line), reflecting a very small relative difference. The red dashed lines correspond to the 95% confidence intervals, while most of the points fell within them, except for a few outliers.

Table 1 presents the results for five healthy subjects and two dysferlinopathy patients at two disease severities. A similar analysis is presented in Section S7, Table S2, for 11 CMT patients. The second column shows the mean T_2 of the water component within the muscle region produced by the extended EMC algorithm along the water/fat fractions. The mean T_2 value of the muscle region for the patients falls within normal range as the T_2 of the diseased muscle ROI averages out when examining the entire muscle region. The VMI is delineated in the third and forth columns representing the relative fraction of viable muscle calculated using the extended EMC algorithm and using the Dixon technique (two- and three-

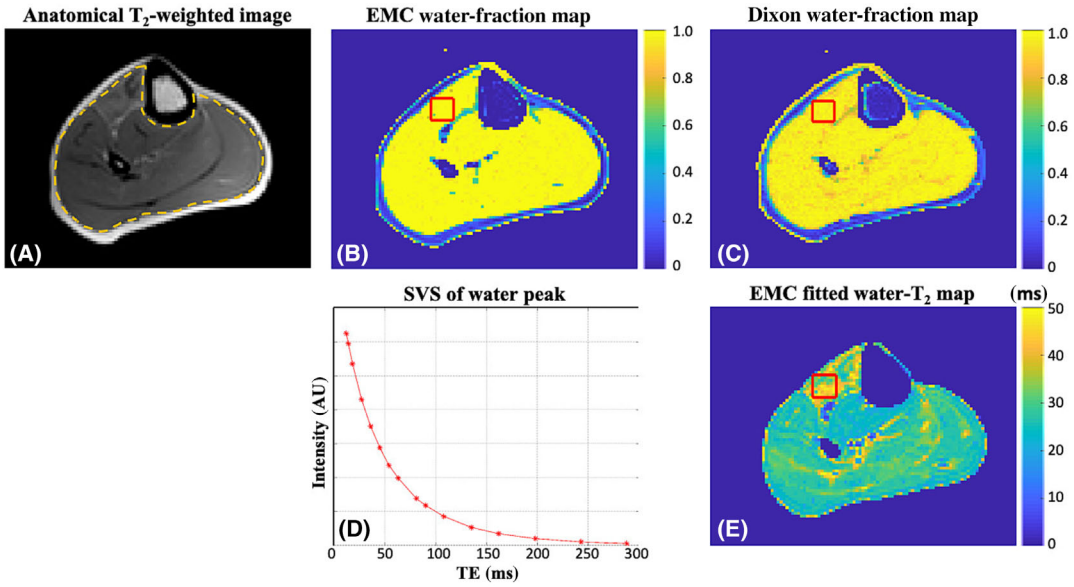

FIGURE 4 Two-T_2 component fit for an axial slice of a calf muscle from the patient with a mild condition of dysferlinopathy. (A) Anatomical T_2- weighted image superimposed with a dashed yellow outline of the muscle mask segmented by the U-Net. (B) f_{water} map from the EMC algorithm with a mean water fraction of $f_W = 96.0\% \pm 8.1\%$ in the muscle region (red ROI). (C) Dixon-based f_{water} map with mean $f_W = 94.0\% \pm 11.0\%$ in the muscle region (red ROI). (D) Exponential decay curve exhibited by the water peak in the spectrums from SVS scans at increasing TEs (diseased muscle region). Exponential fitting produced, in this case, a T_2 value of 42.5 ms. (E) EMC-based T_2^W map for the muscle mask only, with a mean $T_2^W = 38.1 \pm 6.4$ ms (red ROI). EMC, echo modulation curve; ROI, region of interest; SVS, single voxel spectroscopy.

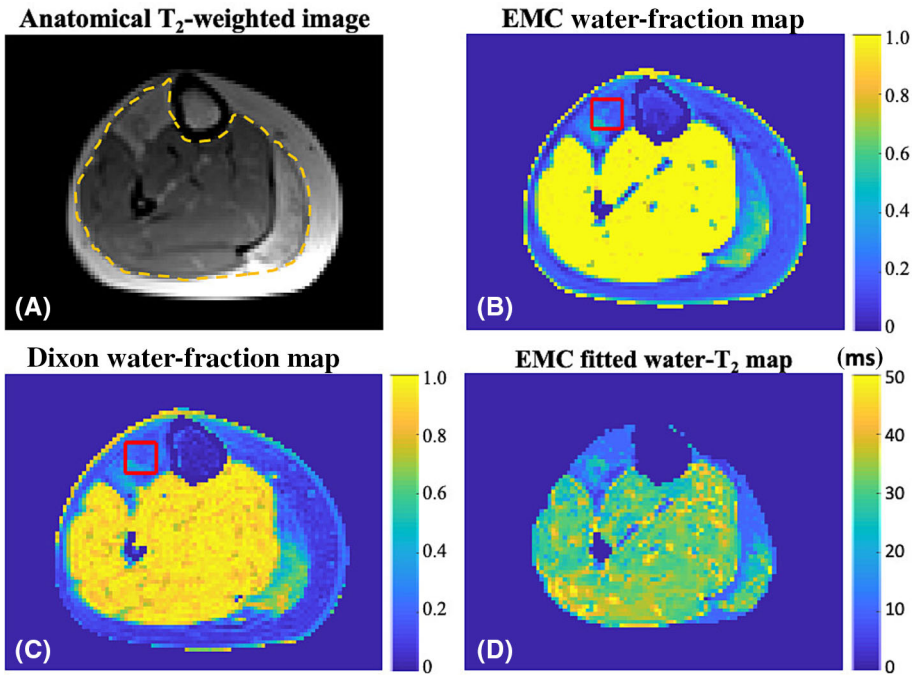

FIGURE 5 Two-T_2 component fit for an axial slice of a calf muscle from the patient with a moderate condition of dysferlinopathy. (A) Anatomical T_2-weighted image superimposed with a dashed yellow outline of the muscle mask, automatically segmented by the U-Net. (B) EMC-based f_{water} map producing a mean water fraction of 22.6% ± 11.5% in the diseased muscle region (red ROI). (C) Dixon-based f_W map producing a mean water fraction of 21.8% ± 8.3% in the diseased muscle region (red ROI). (D) EMC-based water T_2 map. EMC, echo modulation curve; ROI, region of interest.

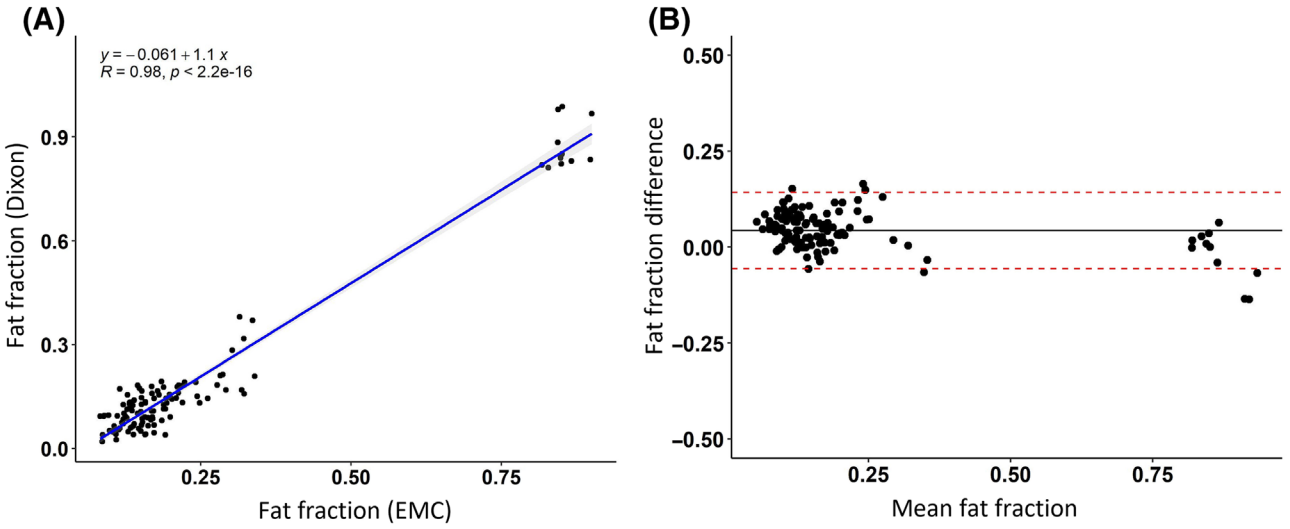

FIGURE 6 (A) Correlation graph of fat fraction (FF) values derived from the extended EMC algorithm and using the gold standard three-point Dixon technique. The two techniques produce highly correlated values ($R^2 = 0.98$, $p < 0.001$). (B) Bland–Altman plot of FF values derived from the extended EMC algorithm and the gold standard three-point Dixon technique, showing high correlation between the two fitting techniques. EMC, echo modulation curve.

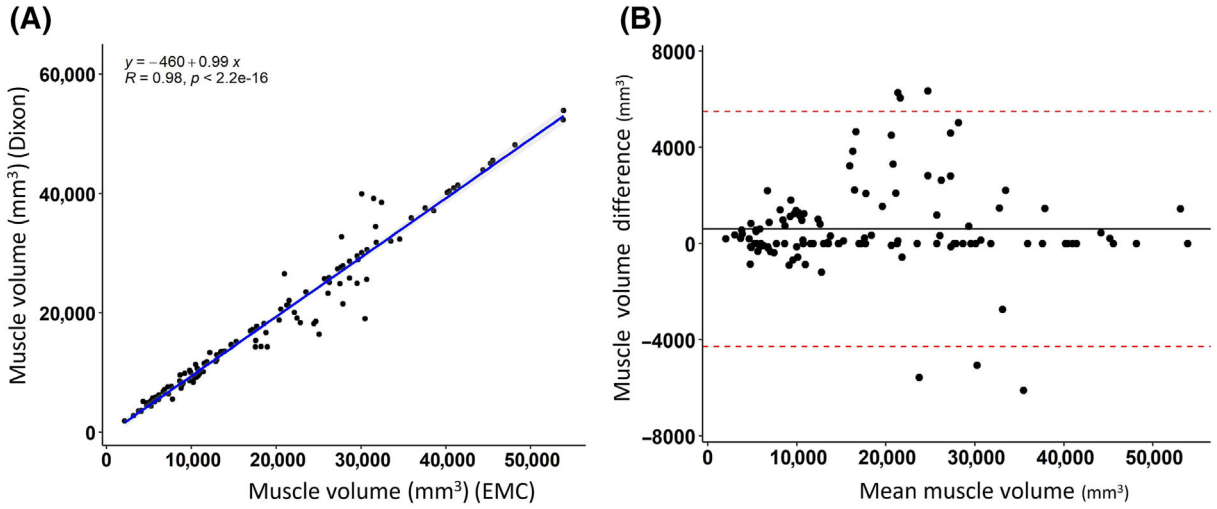

FIGURE 7 (A) Correlation graph of muscle volume values derived from the extended EMC algorithm and using the gold standard three-point Dixon technique. The two techniques produce highly correlated values ($R^2 = 0.98$, $p < 0.001$). (B) Bland–Altman plot of muscle volume values derived from the extended EMC algorithm and the gold standard three-point Dixon technique, showing high correlation between the two fitting techniques. EMC, echo modulation curve.

point Dixon for the volunteers and patients, respectively). Both techniques yielded similar values for the VMI across the five volunteers and two patients. While the patient with moderate dysferlinopathy exhibited a significant reduction in muscle region, this change was not observed in the patient with mild dysferlinopathy. This suggests that although the disease has already set in, the muscle region for this patient has not yet suffered significant tissue degeneration.

This indeed is one of the advantages of using the EMC technique: the measured T_2 values indicate early pathology, even prior to abnormal fat accumulation within the muscle region. The significant tissue degeneration occurs in many cases in a limited tissue region, exhibiting water (muscle) T_2 values that are above normal. Such local elevations, however, are masked when averaging across the entire muscle region as seen from the values in Table 1. Therefore, early detection might, in future work, be based on identifying disease focal points.

Section S7 presents corresponding results for the 11 patients with CMT.

TABLE 1 Comparison of the VMI calculated using the extended EMC algorithm (third column) and using the Dixon technique (forth column) for five healthy subjects (two-point Dixon) and two patients with dysferlinopathy (three-point Dixon). The VMI manifests the fraction of remaining viable muscle out of the entire muscle region where pathology started developing, causing muscle tissue to be replaced by fat. The extended EMC algorithm also yields the mean T_2 within the viable muscle region (second column).

	Extended EMC algorithm		Dixon*
	Mean T_2 (ms)	VMI (%)	VMI (%)
Healthy subject 1	31.9 ± 6.7	97.4	98.8
Healthy subject 2	29.1 ± 4.4	99.4	99.6
Healthy subject 3	33.6 ± 7.8	96.6	95.8
Healthy subject 4	25.8 ± 5.1	92.7	98.8
Healthy subject 5	26.2 ± 4.8	94.8	95.1
Mild patient	27.6 ± 4.7	96.8	100
Moderate patient	28.3 ± 9.4	77.7	81.5

Abbreviations: EMC, echo modulation curve; VMI, viable muscle index.
*Two-point Dixon for volunteers and three-point Dixon for patients.

4 | DISCUSSION

Quantification of fat infiltration and its accumulation in diseased muscle regions has a high prognostic value, enabling to assess tissue status and monitor the progression of muscle dystrophies and neuromuscular disorders.[30] This, however, requires accurate identification and separation of the fat and water components.

Several techniques exist for separating water and fat, with Dixon being considered the gold standard.[7] Despite its widespread use, this technique has several limitations. First, the two-point Dixon technique does not account for inhomogeneities of the external main and transmit magnetic fields (B_0 and B_1^+). This is partially rectified by using the three-point Dixon technique, which accounts for B_0 inhomogeneities by acquiring a third image.[8] The EMC algorithm does not suffer from B_0 inhomogeneities as it is based on a SE protocol. It also eliminates $B_1{}^+$ inhomogeneities as their effect is modeled in the fitting process.[14] Second, Dixon might misclassify water as fat, and vice versa, when their relative fractions are close to 50%.[31,32] This is because the water component decays very quickly relative to the fat, hence even for a relatively high fraction of the water component, its signal intensity would be low and only make a small contribution to the overall acquired signal, leading to water-fat misclassifications.

In this study we introduced an extension to the EMC T_2-mapping algorithm,[15,16,23] which allows to separate the water and fat components within each imaged voxel based on their transverse relaxation time constants. The outputs are maps of water T_2 values T_2^W, and the relative fractions of water and fat (f_W, f_F). Further to that, the EMC technique employs a standard MESE protocol scheme, making it readily available on any clinical or preclinical scanner. Another technique that is based on MESE protocols for mapping T_2 is the slice-resolved extended phase graph (SR-EPG) algorithm.[33] These techniques provide different performances, and particularly with respect to the use of non-180° refocusing pulses. A rigorous comparison of Bloch simulations-based T_2 mapping to EPG-based T_2 mapping showed that the former is more robust to $B_1{}^+$ inhomogeneities (see McPhee and Wilman[34]). Another added value of the EMC approach is its use of the exact pulse-sequence timing diagram in the Bloch simulations of the MESE signals, producing values that are more reproducible across different scanners and scan settings.[23,35] A further comparison of EMC-based and EPG-based fat/water separation would be of interest, but is beyond the scope of the current study.

By using quantitative T_2 mapping, one can obtain both global and quantitative assessment of the disease state. The globality arises by automatically analyzing data from the entire calf and thigh muscles, and not just from representative ROIs. The quantitative values include the relaxation times of both the fat and muscle (i.e., water) components, their relative fractions, and a complementary clinical biomarker, the VMI, representing the percentage of the remaining muscle tissue. This has the potential to enhance diagnosis accuracy, improve patient follow-up, and reduce observer-dependent bias in decision-making processes.[23,36] The extended EMC method shows promising results, yielding an average muscle T_2 of 29.3 ± 3.4 ms for all the healthy subjects, consistent with literature values, for example, Kršňák et al., who reported T_2 of 30 ms in the muscle, and Gold et al., who reported T_2 of 31.7 ± 1.9 ms.[37,38] Analyzing patients' data, we saw that the VMI decreased with disease severity as more fat replaces the diseased muscle tissue. Further, more rigorous validation is needed, comparing the VMI's values vis-à-vis radiologic grading of the disease on large patient populations. Furthermore, the result shown for the dysferlinopathy patient in Figure 4, where the T_2 of the muscle increases prior to fat replacement, is consistent with previous reports where increased T_2 was shown to be a sensitive biomarker for the level of pathology caused, for example, by inflammation, edema, or necrosis of dystrophic cell lesions.[11,39]

The measurement of disease progression and therapeutic responses is most accurately done by taking a muscle biopsy and quantifying the proteins responsible for the disease.[40,41] The expression of dystrophin, the protein product of several muscular dystrophies, has been used as an

outcome measure in clinical trials.[42] However, accurate quantification of dystrophin has been challenging and requires an invasive muscle biopsy.[43] Some pitfalls of performing a muscle biopsy are that it is an invasive surgical procedure performed under a local anesthetic, it cannot be applied repetitively, and it is spatially localized and hence less indicative of the entire tissue state.[44] MRI's measure of the water transverse relaxation time (T_2) has been shown to correlate with dystrophin expression and to therapeutic efficiency in a dog model of Duchenne muscle dystrophy.[45] Hence, noninvasively monitoring the T_2 of muscle, that is, of the water components, has the potential to provide additional insight to the tissue's biochemical state.

The early detection of neuromuscular disorders is of significant importance, because the only way to slow down the progression of these disorders is to treat the diseased muscle tissue prior to the infiltration of fat. Once fat infiltration crosses a certain threshold, the disease is considered to be too advanced and there is not much physicians can do. qMRI's transverse relaxation time provides, in this case, an effective and early marker of the muscle status and treatment response. Adding this value to the standard fat/water fraction may thus assist physicians in the early detection of neuromuscular disorders.

Notwithstanding its advantages, the extended EMC algorithm is still limited when analyzing water content and T_2 values in muscle tissues where fat levels are 50% and above. The very low water content in these regions, combined with their short T_2 relaxation times (~30 ms), leads to very low SNR of the water signal and makes it challenging to quantify these values, particularly when using MESE protocols which are limited to sampling the time domain with an echo spacing of 8–10 ms and above. Such conditions emerge at severely diseased regions, leading to ambiguities in the three-parameter fit, where several EMCs with different $\left[T_2^W, T_2^F, f_W\right]$ values may produce similar decay curves. We believe that this is not highly limiting from a clinical perspective because at such advanced disease levels the clinically relevant parameter is actually the relative fraction of fat and the volume of remaining muscle tissue. The three-parameter fitting process also had ambiguity, which was overcome by fixing the fat T_2 value to its value at the SC fat region (step (c) in the extended EMC algorithm) and introducing it as a known input in step (d) of the algorithm (Figure 1). A central assumption in our study is that once disease sets in, the entire muscle is affected, and no muscle region can be considered genuinely healthy. One can only state that the disease does not yet show on MR images in some parts of the muscle. SC fat was therefore chosen as a stable reference point that is assumed not to change as the disease appears and progresses. Another potential limitation of using a MESE protocol is magnetization transfer (MT) effects that might influence water and fat differently. It was previously shown that these can attenuate the water signal, and while having little effect on the estimated T_2 value,[46] they can potentially bias the relative fraction measured for fat and for water depending on the saturation efficiency and transfer rate of each component. Investigation of this mechanism and its integration into the extended EMC processing is part of an ongoing analysis of MT effects.

Contrary to analyzing signals with low water contents, two-component fitting algorithms are able to estimate very low levels of fat because of the relatively high SNR of this component. This is for two reasons. First, fat has a relatively long T_2, allowing to sample a large number of timepoints before its signal drops below the noise level. Second, the longitudinal T_1 relaxation time of fat is relatively short, ~365 ms, compared with muscle, which is ~1400 ms.[47,48] Fat's longitudinal magnetization thus recovers very efficiently between each TR, resulting in higher steady state signal levels.

The EMC's fitting process is performed via a three-parameter exhaustive search, scanning over the physiological ranges of the T_2^W, T_2^F, and f_W parameters. The resulting fitting time is ~1 min per slice on a standard PC (see Section S4). Other, more sophisticated, optimization algorithms (such as Monte Carlo or gradient descent search schemes) could be used to decrease the computation time.[49] The drawback of such algorithms is that most of them rely on a convex search space with one global minimum, which may lead to finding a local, rather than the global, minimum. We thus chose the exhaustive, yet robust approach, in this proof-of-principle study, and employed parallel computing to decrease the overall fitting time.

The two-component EMC fitting technique can be extended to other tissues, including the quantification of fat in fatty liver disease,[50] early detection of multiple sclerosis via quantification of the myelin component,[51,52] imaging luminal water for the detection of prostate cancer,[51] and the differentiation between fat and glandular tissue and lesions for early detection of breast cancer.[53]

The FCNN's ground truth muscle and SC fat maps were delineated by an expert with more than 10 years of experience. The entire development process is described in Amer et al.[26,54] A more rigorous development process where multiple experts provide the ground truth might have produced a more robust network. Previous work, however, used one expert for ground truth, while similar applications have been shown to perform well.[54–58]

The fat component in the extended EMC algorithm was assumed to originate only from the methylene peak of the fat molecule. This is a limitation of this study because although this is the most abundant peak, the full fat spectrum contains other, smaller peaks. Future work is required to expand the EMC algorithm to model multipeak signals.

5 | CONCLUSIONS

This work demonstrated the utility of the extended EMC algorithm as a tool for accurately quantifying the relative fat and water in muscle tissues in addition to producing quantitative parametric maps of muscle and fat T_2 values. The ensuing framework provides values that are stable across

scanner and scan settings and includes automated muscle segmentation and the VMI biomarker calculation, offering a global and quantitative tool for staging and monitoring neuromuscular dystrophies.

ACKNOWLEDGMENTS

This research was funded by the ISF Grant 2009/17, and the CNRS and APHM. The authors have no other conflicts of interest to declare.

ORCID

David Bendahan https://orcid.org/0000-0002-1502-0958
Noam Ben-Eliezer https://orcid.org/0000-0003-2944-6412

REFERENCES

1. Mercuri E, Pichiecchio A, Allsop J, Messina S, Pane M, Muntoni F. Muscle MRI in inherited neuromuscular disorders: Past, present, and future. *J Magn Reson Imaging*. 2007;25(2):433-440. doi:10.1002/jmri.20804
2. Gloor M, Fasler S, Fischmann A, et al. Quantification of fat infiltration in oculopharyngeal muscular dystrophy: Comparison of three MR imaging methods. *J Magn Reson Imaging*. 2011;33(1):203-210. doi:10.1002/jmri.22431
3. Schick F, Eismann B, Jung WI, Bongers H, Bunse M, Lutz O. Comparison of localized proton NMR signals of skeletal muscle and fat tissue in vivo: Two lipid compartments in muscle tissue. *Magn Reson Med*. 1993;29(2):158-167. doi:10.1002/mrm.1910290203
4. Bley TA, Wieben O, François CJ, Brittain JH, Reeder SB. Fat and water magnetic resonance imaging. *J Magn Reson Imaging*. 2010;31(1):4-18. doi:10.1002/jmri.21895
5. Carlier PG, Azzabou N, de Sousa PL, et al. Skeletal muscle quantitative nuclear magnetic resonance imaging follow-up of adult Pompe patients. *J Inherit Metab Dis*. 2015;38(3):565-572. doi:10.1007/s10545-015-9825-9
6. Ma J. Dixon techniques for water and fat imaging. *J Magn Reson Imaging*. 2008;28(3):543-558. doi:10.1002/jmri.21492
7. Dixon TW. Simple proton spectroscopic imaging. *Radiology*. 1984;153:189-194. doi:10.1148/radiology.153.1.6089263
8. Glover GH, Schneider E. Three-point Dixon technique for true water/fat decomposition with B0 inhomogeneity correction. *Magn Reson Med*. 1991;18(2):371-383. doi:10.1002/mrm.1910180211
9. Kan HE, Scheenen TWJ, Wohlgemuth M, et al. Quantitative MR imaging of individual muscle involvement in facioscapulohumeral muscular dystrophy. *Neuromuscul Disord*. 2009;19(5):357-362. doi:10.1016/j.nmd.2009.02.009
10. Friedman SD, Poliachik SL, Carter GT, Budech CB, Bird TD, Shaw DWW. The magnetic resonance imaging spectrum of facioscapulohumeral muscular dystrophy. *Muscle Nerve*. 2012;45(4):500-506. doi:10.1002/mus.22342
11. Carlier PG. Global T2 versus water T2 in NMR imaging of fatty infiltrated muscles: Different methodology, different information and different implications. *Neuromuscul Disord*. 2014;24(5):390-392. doi:10.1016/j.nmd.2014.02.009
12. Azzabou N, De Sousa PL, Caldas E, Carlier PG. Validation of a generic approach to muscle water T2 determination at 3T in fat-infiltrated skeletal muscle. *J Magn Reson Imaging*. 2015;41(3):645-653. doi:10.1002/jmri.24613
13. Hennig J. Multiecho imaging sequences with low refocusing flip angles. *J Magn Reson*. 1988;78(3):397-407. doi:10.1016/0022-2364(88)90128-X
14. Radunsky D, Stern N, Nassar J, Tsarfaty G, Blumenfeld-Katzir T, Ben-Eliezer N. Quantitative platform for accurate and reproducible assessment of transverse (T2) relaxation time. *NMR Biomed*. 2021;34(8):e4537. doi:10.1002/nbm.4537
15. Ben-Eliezer N, Sodickson DK, Shepherd T, Wiggins GC, Block KT. Accelerated and motion-robust in vivo T 2 mapping from radially undersampled data using Bloch-simulation-based iterative reconstruction. *Magn Reson Med*. 2016;75(3):1346-1354. doi:10.1002/mrm.25558
16. Ben-Eliezer N, Sodickson DK, Block KT. Rapid and accurate T2 mapping from multi-spin-echo data using bloch-simulation-based reconstruction. *Magn Reson Med*. 2015;73(2):809-817. doi:10.1002/mrm.25156
17. Hennig J, Weigel M, Scheffler K. Calculation of flip angles for echo trains with predefined amplitudes with the extended phase graph (EPG)-algorithm: principles and applications to hyperecho and TRAPS sequences. *Magn Reson Med*. 2004;51(1):68-80. doi:10.1002/mrm.10658
18. Marty B, Baudin PY, Reyngoudt H, et al. Simultaneous muscle water T2 and fat fraction mapping using transverse relaxometry with stimulated echo compensation. *NMR Biomed*. 2016;29(4):431-443. doi:10.1002/nbm.3459
19. Keene KR, Beenakker JWM, Hooijmans MT, et al. T2 relaxation-time mapping in healthy and diseased skeletal muscle using extended phase graph algorithms. *Magn Reson Med*. 2020;84(5):2656-2670. doi:10.1002/mrm.28290
20. Ma D, Gulani V, Seiberlich N, et al. Magnetic resonance fingerprinting. *Nature*. 2013;495(7440):187-192. doi:10.1038/nature11971
21. Körzdörfer G, Jiang Y, Speier P, et al. Magnetic resonance field fingerprinting. *Magn Reson Med*. 2019;81(4):2347-2359. doi:10.1002/mrm.27558
22. Cencini M, Biagi L, Kaggie JD, Schulte RF, Tosetti M, Buonincontri G. Magnetic resonance fingerprinting with dictionary-based fat and water separation (DBFW MRF): A multi-component approach. *Magn Reson Med*. 2019;81(5):3032-3045. doi:10.1002/mrm.27628
23. Shepherd TM, Kirov II, Charlson E, et al. New rapid, accurate T2 quantification detects pathology in normal-appearing brain regions of relapsing-remitting MS patients. *NeuroImage Clin*. 2017;14:363-370. doi:10.1016/j.nicl.2017.01.029
24. Tal A, Gonen O. Spectroscopic localization by simultaneous acquisition of the double-spin and stimulated echoes. *Magn Reson Med*. 2015;73(1):31-43. doi:10.1002/mrm.25112
25. Kingma DP, Ba J. Adam: A Method for Stochastic Optimization. Published online. 2014:1-15. arXiv:1412.6980.
26. Amer R, Nassar J, Bendahan D, Greenspan HBEN. Automatic Segmentation of Muscle Tissue and Inter-muscular Fat in Thigh and Calf MRI Images. In: *Med Image Comput Comput Assist Interv – MICCAI*. Springer; 2019:11765.
27. FSLeyes|Zenodo. Accessed May 1, 2022. https://zenodo.org/record/5576035#.Ym6d7e3MI2x
28. Bornewasser M. Vernetztes Kompetenzmanagement - Anforderungen und Ausblick. In: Vernetztes Kompetenzmanagement. Springer; 2018;187-194.
29. Ronneberger O, Fischer P, Brox T. U-Net: Convolutional networks for biomedical image segmentation. *Lect Notes Comput Sci Subser Lect Notes Artif Intell Lect Notes Bioinforma*. 2015;9351:234-241. doi:10.1007/978-3-319-24574-4_28

30. Morrow JM, Sinclair CDJ, Fischmann A, et al. MRI biomarker assessment of neuromuscular disease progression: A prospective observational cohort study. *Lancet Neurol*. 2016;15(1):65-77. doi:10.1016/S1474-4422(15)00242-2
31. Ladefoged CN, Hansen AE, Keller SH, et al. Impact of incorrect tissue classification in Dixon-based MR-AC: fat-water tissue inversion. *EJNMMI Phys*. 2014;1(1):101. doi:10.1186/s40658-014-0101-0
32. Basty N, Thanaj M, Cule M, et al. Swap-Free Fat-Water Separation in Dixon MRI using Conditional Generative Adversarial Networks. *ArXiv210714175 Cs Eess*. Accessed May 4, 2022. http://arxiv.org/abs/2107.14175
33. Lebel RM, Wilman AH. Transverse relaxometry with stimulated echo compensation. *Magn Reson Med*. 2010;64(4):1005-1014. doi:10.1002/mrm.22487
34. McPhee KC, Wilman AH. Transverse relaxation and flip angle mapping: Evaluation of simultaneous and independent methods using multiple spin echoes. *Magn Reson Med*. 2017;77(5):2057-2065. doi:10.1002/mrm.26285
35. Cosi V, Yoshimoto A, Shepherd T, Block K, Sodickson D, Ben-Eliezer N. Fast and Accurate T2 Mapping from Multi Spin Echo Data Using Bloch-Simulation-Based Reconstruction: Investigation of intra-subject and inter-scan stability and reproducibility. Proc of the 24th Intr Soc Magn Reson Med, Singapore; 2016:4824.
36. Lareau-Trudel E, Le TA, Ghattas B, Pouget J. Muscle quantitative MR imaging and clustering analysis in patients with facioscapulohumeral muscular dystrophy type 1. *PLoS ONE*. 2015;(1):1-16. doi:10.1371/journal.pone.0132717
37. Kršňák M, Lindeboom L, Schrauwen-Hinderling V, et al. Proton magnetic resonance spectroscopy in skeletal muscle: Experts' consensus recommendations. *NMR Biomed*. 2021;34(5):e4266. doi:10.1002/nbm.4266
38. Gold GE, Han E, Stainsby J, Wright G, Brittain J, Beaulieu C. Musculoskeletal MRI at 3.0 T: relaxation times and image contrast. *Am J Roentgenol*. 2004;183(2):343-351. doi:10.2214/ajr.183.2.1830343
39. Triplett WT, Baligand C, Forbes SC, et al. Chemical shift-based MRI to measure fat fractions in dystrophic skeletal muscle. *Magn Reson Med*. 2014;72(1):8-19. doi:10.1002/mrm.24917
40. Buchthal F, Kamieniecka Z. The diagnostic yield of quantified electromyography and quantified muscle biopsy in neuromuscular disorders. *Muscle Nerve*. 1982;5(4):265-280. doi:10.1002/mus.880050403
41. Joyce NC, Oskarsson B, Jin LW. Muscle biopsy evaluation in neuromuscular disorders. *Phys Med Rehabil Clin N Am*. 2012 Aug;23(3):609-631. doi:10.1016/j.pmr.2012.06.006
42. Hoffman EP, Brown RH, Kunkel LM. Dystrophin: The protein product of the Duchenne muscular dystrophy locus. *Cell*. 1987;51(6):919-928. doi:10.1016/0092-8674(87)90579-4
43. Anthony K, Arechavala-Gomeza V, Taylor LE, et al. Dystrophin quantification: Biological and translational research implications. *Neurology*. 2014;83(22):2062-2069. doi:10.1212/WNL.0000000000001025
44. Dubowitz V, Caroline AS, Oldfors A. Muscle biopsy: a practical approach: expert consult. W.B. Saunders; 2014. doi:10.1016/B978-0-7020-4340-6.00002-1
45. Yokota T, Lu QL, Partridge T, et al. Efficacy of systemic morpholino exon-skipping in Duchenne dystrophy dogs. *Neurology*. 2009;65(6):667-676.
46. Radunsky D, Blumenfeld-Katzir T, Volovyk O, et al. Analysis of magnetization transfer (MT) influence on quantitative mapping of T2 relaxation time. *Magn Reson Med*. 2019;82(1):145-158. doi:10.1002/mrm.27704
47. Han E, Gold G, Stainsby J, Wright G, Beaulieu C, Brittain J. T1 and T2 Measurements of Muskuloskeletal Tissue at 3T and 1.5T. *Proc 11th ISMRM Sci Meet*. 2003;11:450.
48. Karampinos DC, Yu H, Shimakawa A, Link TM, Majumdar S. T 1-corrected fat quantification using chemical shift-based water/fat separation: Application to skeletal muscle. *Magn Reson Med*. 2011;66(5):1312-1326. doi:10.1002/mrm.22925
49. Shpringer G, Ben-Eliezer N. Accelerated reconstruction of T2 maps based on the echo modulation curve signal model, and using PCA and gradient-descent search algorithms. In: ISMRM, 28th Annual Meeting. ISMRM; 2020.
50. Tang A, Tan J, Sun M, et al. Nonalcoholic fatty liver disease: MR imaging of liver proton density fat fraction to assess hepatic steatosis. *Radiology*. 2013;267(2):422-431. doi:10.1148/radiol.12120896
51. Devine W, Giganti F, Johnston EW, et al. Simplified luminal water imaging for the detection of prostate cancer from multiecho T2 MR images. *J Magn Reson Imaging*. 2019;50(3):910-917. doi:10.1002/jmri.26608
52. Omer N, Galun M, Stern N, Blumenfeld-Katzir T, Ben-Eliezer N. Data-driven algorithm for myelin water imaging: Probing subvoxel compartmentation based on identification of spatially global tissue features. *Magn Reson Med*. 2021;87(5):2521-2535. doi:10.1002/mrm.29125
53. Harms E, Flamig P, Evans WP, et al. Fat-suppressed imaging of the breast. *Radiographics*. 1993;13(2):247-267. doi:10.1148/radiographics.13.2.8460218
54. Amer R, Nassar J, Trabelsi A, Bendahan D, Greenspan H, Ben-Eliezer N. Quantification of intra-muscular adipose infiltration in calf/thigh MRI using fully and weakly supervised semantic segmentation. *Bioengineering*. 2022;9(7):315. doi:10.3390/bioengineering9070315
55. Positano V, Christiansen T, Santarelli MF, Ringgaard S, Landini L, Gastaldelli A. Accurate segmentation of subcutaneous and intermuscular adipose tissue from MR images of the thigh. *J Magn Reson Imaging*. 2009;29(3):677-684. doi:10.1002/jmri.21699
56. Valentinitsch A, Karampinos DC, Alizai H, et al. Automated unsupervised multi-parametric classification of adipose tissue depots in skeletal muscle. *J Magn Reson Imaging*. 2013;37(4):917-927. doi:10.1002/jmri.23884
57. Orgiu S, Lafortuna CL, Rastelli F, Cadioli M, Falini A, Rizzo G. Automatic muscle and fat segmentation in the thigh from T1-weighted MRI. *J Magn Reson Imaging*. 2016;43(3):601-610. doi:10.1002/jmri.25031
58. Barnouin Y, Butler-Browne G, Voit T, et al. Manual segmentation of individual muscles of the quadriceps femoris using MRI: A reappraisal. *J Magn Reson Imaging*. 2014;40(1):239-247. doi:10.1002/jmri.24370

SUPPORTING INFORMATION

Additional supporting information can be found online in the Supporting Information section at the end of this article.

How to cite this article: Nassar J, Trabelsi A, Amer R, et al. Estimation of subvoxel fat infiltration in neurodegenerative muscle disorders using quantitative multi-T_2 analysis. *NMR in Biomedicine*. 2023;e4947. doi:10.1002/nbm.4947